Enhanced Oxygen Evolution Catalysis by Aluminium-Doped Cobalt Phosphide Through *In Situ* Surface Area Increase

Timothy E. Rosser,[a] Juliana P. S. Sousa,[b] Yasmine Ziouani,[b] Oleksandr Bondarchuk,[b] Dmitri Y. Petrovykh,[b] Xian-Kui Wei,[c] Jo. J. L. Humphrey,[a] Marc Heggen,[c] Yury V. Kolen'ko,*[b] and Andrew J. Wain*[a]

[a] National Physical Laboratory, Hampton Road, Teddington, Middlesex TW11 0LW, UK.

E-mail: andy.wain@npl.co.uk

[b] International Iberian Nanotechnology Laboratory, Braga 4715-330, Portugal.

E-mail: yury.kolenko@inl.int

[c] Ernst Ruska-Centre for Microscopy and Spectroscopy with Electrons and Peter Grünberg Institute, Forschungszentrum Jülich GmbH, 52425 Jülich, Germany.

Abstract

The deployment of water electrolysis as a major contributor to global hydrogen production requires the elimination of catalysts based on scarce and expensive precious metals, and amongst the most promising alternatives are first-row transition metal phosphides. This study presents the synthesis, characterisation, electrochemical testing and performance rationalisation of cobalt phosphide modified with aluminium as an improved catalyst for alkaline oxygen evolution. The electrodes were prepared by gas phase phosphorisation of Al-sputtered Co foam, and characterised by SEM, EDX, XRD, XPS, HAADF-STEM and Raman spectroscopy. Al modification enhances the oxygen evolution performance of the anodes, with a current density of 200 mA cm^{-2} reached at an overpotential of 360 mV, representing a 50 mV improvement compared to the Al-free sample. Double layer capacitance measurements indicate that the performance enhancement results from an approximately four-fold increase in relative electrochemically active surface area (ECSA) in the Al-modified sample. *In situ* Raman spectroscopy rationalises this ECSA increase on the grounds of an Al-induced preference for a spinel phase Co/Al oxide on the catalyst surface upon exposure to electrolyte solution, the compact crystal structure of which causes shrinkage and surface cracking. This contrasts previous observations on Al-doped nickel phosphides, where an increase in surface area was attributed to Al dissolution. These results present a route for achieving high current density oxygen evolution without the need to alter the catalyst active species, as well as demonstrate the importance of *in situ* techniques for rationalising performance improvements resulting from subtle differences in surface chemistry.

1. Introduction

Electrochemical water splitting is one of the most mature technologies for generating pure H_2 and is a very attractive means to store electrical energy in the form of chemical bonds, with the potential for more sustainable power generation with reduced CO_2 emissions when released through combustion or a fuel cell. Water splitting electrolysis consists of two half reactions, the H_2 evolution reaction (HER) at the cathode and the O_2 evolution reaction (OER) at the anode, both of which require catalysts to reduce kinetic barriers and maximise energy efficiency. Platinum group metal (PGM) based materials (e.g., Pt, IrO_2, RuO_2, $IrRuO_x$) are the most prevalent catalysts for acidic water splitting owing to their high activity and stability, however, they suffer the drawbacks of low natural abundance and availability, and high cost. Therefore, replacing PGM catalysts with more earth-abundant materials offering competitive activity is a key challenge. Alkaline electrolysis negates the requirement for PGMs, with Ni-based catalysts finding widespread application due to their stability under high pH conditions. However, further improvements are sought, with efforts focusing on both enhancing the intrinsic catalytic activity and increasing the exposed surface area of these catalysts to maximise performance.

Recent studies by our group and other researchers have identified transition metal phosphides as a viable alternative to PGMs as catalysts for acid/alkaline water electrolysis.[1–9] They can be prepared by phosphorisation of metal foams, offering self-supporting electrodes with high macroscopic surface area, and therefore produce the high current densities at low overpotentials required for industrial application.[2] It has previously been observed that modification of these materials with Al increases their activity, such as Al−Ni−P foam cathodes prepared by alloying of Ni and Al followed by phosphorisation.[3] The resulting cathode demonstrated significantly lower overpotentials for acidic HER as compared to the Al-free Ni−P cathode. The Al modification concept has been extended to highly active anodes for alkaline OER.[1] After modification of a Ni−P foam with Al, the resultant anode exhibited impressive current densities of 10, 100, and 300 mA cm^{-2} at low overpotentials of 180, 247, and 312 mV, respectively. A principal route by which Al modification was reported to enhance anode performance was through alkaline leaching of Al-containing phases during OER, which led to an increase in surface area and porosity compared to the Al-free case, and thus higher performance per unit of geometric area.

Several recent studies have revealed that phosphides of Co also exhibit high HER and OER activity,[7,10–14] including those doped with Al.[15,16] In order to explore the Al modification phenomenon further, in this work we prepared Co analogues to the above Ni phosphides and investigated their potential application as OER catalysts under alkaline conditions. As well as exhibiting a performance enhancement as a result of Al-modification, these materials offered the advantage of strong Raman-active vibrational modes (compared to weak bands observed for Ni−P), allowing surface speciation to be monitored spectroscopically under *in situ* and *operando* conditions.

2. Experimental

2.1. Starting Materials

Metallic Co foam (110 pores per inch, Heze Jiaotong), Al and Co sputtering targets (Materion), red P powder (98.9%, Alfa Aesar), 37% HCl (Carlo Erba), KOH (≥85%, Sigma-Aldrich) and Pt wire (99.9%, Sigma-Aldrich) were obtained from commercial suppliers. Ultrapure water (18.2 MΩ cm, TOC < 3 ppb) was produced using a Milli-Q Advantage A10 system (Millipore).

2.2. Preparation of Electrodes

The desired Al-modified Co−P foams and control Co−P (abbreviated as **AlCoP** and **CoP**, respectively) were synthesised *via* a gas transport phosphorisation route, adapted from the method developed previously for the synthesis of Al-modified Ni-P electrodes.[3] Co foams were cleaned by ultrasonication in 6 M HCl aqueous solution for 5 min to remove the surface oxide layer, followed by washing with water and acetone, and finally dried using a flow of N_2. The phase purity of the product after acidic cleaning was confirmed by powder X-Ray Diffraction (XRD). According to the XRD, the commercial cobalt foam was a phase mixture of metallic hexagonal (ICDD no. 00-005-0727, $P6_3/mmc$) and cubic (ICDD no. 04-006-8067, $Fm\text{-}3m$) cobalt.

A 500 nm Al layer was deposited onto both sides of the Co foam piece (10 × 10 cm^2) by sputtering in a Four-Target-Module system (Singulus Technologies). The successful deposition of Al was confirmed by XRD and gave the foam a silver appearance. Subsequently, to sandwich the Al layer, a 30 nm layer of Co was sputtered onto both sides of the Al/Co foam using a multitarget ultrahigh vacuum sputtering system (Kenosistec). Finally, the resulting grey Co/Al/Co composite foam was stored in a desiccator under vacuum.

Prior to phosphorisation, the Co/Al/Co composite foam was subjected to heat treatment under an inert argon atmosphere to achieve good physical mixing between Al and Co and to ensure good adhesion between sputtered Co/Al layers and pristine Co foam. For heat treatment, the Co/Al/Co foam was cut into 2.4 × 5 cm^2 pieces and then was heated to 600 °C at 5 °C min^{-1}, kept at this temperature for 2 h, then slowly cooled down to 500 °C at 0.5 °C min^{-1}, and finally cooled to room temperature in the furnace. The heat treatment was conducted under argon gas flow of 50 mL min^{-1} using a tube furnace (Lenton), equipped with a quartz tube (QSIL). The as-produced Co/Al/Co foam was stored in a desiccator under vacuum.

The final self-supported electrodes were obtained by gas-transport phosphorisation method. For this purpose, 0.5 g of red P was loaded into an alumina combustion boat and placed at the beginning of the heated zone of a tube furnace (Lenton), equipped with a quartz tube (QSIL). Next, a 2.4 × 5 cm^2 piece of heat-treated foam was placed in the middle of the heated zone of the furnace. The distance between the red P and the foam was approximately 3 cm. The phosphorisation was conducted under a flow of

argon at 50 mL min^{-1}. The system was heated to 500 °C at 10 °C min^{-1} and kept at this temperature for 6 h. Finally, the system was cooled down to 250 °C at 10 °C min^{-1} and kept at this temperature for 12 h. Important note: At high temperature (> 300 °C), P red transforms into P yellow, which is highly volatile, toxic, and pyrophoric. Hence, the last treatment at 250 °C for 12 h is required to convert yellow P back to the inert red form. Through the gas-transport reaction between the electropositive metal and electronegative phosphorus, the self-supported grey/black Al-modified cobalt phosphide foam electrode was obtained (abbreviated as **AlCoP**). The mass difference between the as-prepared **AlCoP** and **CoP** foams was measured to be approximately 1 mg, and therefore negligible compared to the overall mass of the foams.

For comparison, a reference binary Co–P foam anode was also synthesised. The sample was prepared mimicking the synthesis of **AlCoP**, but omitting the Al sputtering step. The resultant self-supported cobalt phosphide foam is abbreviated as **CoP**.

2.3. Electrocatalytic Tests

Electrochemical water oxidation experiments were carried out at 22 °C in a three-electrode assembly using a geometrically well-defined piece of self-supported **AlCoP** or control **CoP** foam anodes, a Pt wire as the counter electrode and a saturated calomel electrode (SCE) as the reference electrode (no adventitious chloride was detected in any of the analytical measurements performed). The electrolyte was aq. 1.0 M KOH. For comparison, the electrocatalytic performance of clean pristine Co foam was also evaluated. The measurements were performed with a potentiostat/galvanostat (VMP-3, Biologic) while carrying out cyclic voltammetry (CV) at 5 mV s^{-1} in the potential range of 1.2 V to 1.8 V *versus* reversible hydrogen electrode (RHE), applying 85% internal resistance compensation. The voltage drop (*iR*) was measured by single-point high frequency (100 kHz) impedance measurements. Data presented was obtained after 20 initial CV cycles, during which the electrochemical response was observed to stabilise and no significant change in OER overpotential was observed during this period. The stability test was performed using galvanostatic electrolysis at a fixed current density of 10 mA cm^{-2} while monitoring the variation of potential E / V_{RHE} for 150 h. These stability test conditions were used to prepare samples for XRD, XPS and EDX post-catalysis measurements.

Comparison data for IrO_2 and RuO_2 catalysts were obtained from reference 17, in which catalysts were deposited on Ni foam current collectors and were cycled under the same conditions as described above.

The relative electrochemically active surface area (ECSA) of the solid–electrolyte interface of the electrodes was assessed on the basis of geometric double-layer capacitance, C_{dl}, measurements. CV cycles were recorded from 1.17 V_{RHE} to 1.27 V_{RHE} for **AlCoP** and control **CoP** foam electrodes under the standard conditions of alkaline OER experiment using increasing scan rates of 5, 10, 25, 50, 75, 100, 125, 150, 175, and 200 mV s^{-1}. A linear trend is obtained *via* plotting half the difference in current

density (j) between the anodic and cathodic sweeps, ($j_{anodic} - j_{cathodic}$) / 2, in the non-Faradaic region of the cyclic voltammograms (≈1.2 V_{RHE}) as a function of the scan rate. The slope of the linear fitting of these data is the geometric double-layer capacitance, C_{dl} / mF cm^{-2}, which is linearly proportional to the ECSA for a given surface. The ratio between C_{dl} of **AlCoP** and **CoP** anodes was used as an estimate of the relative ECSA.

2.4. Characterisation methods

2.4.1. Powder X-ray Diffraction

Powder X-ray diffraction (XRD) data were collected on an X'Pert PRO diffractometer (PANalytical) set at 45 kV and 40 mA, and equipped with Cu K_α radiation (λ = 1.541874 Å) and a PIXcel detector. Data were collected using Bragg-Brentano geometry in the 20° to 80° 2θ range with a scan speed of 0.01° s^{-1}. The XRD patterns were matched to International Centre for Diffraction Data (ICDD) PDF-4 database using HighScore software package (PANalytical) and are reported here after background subtraction and adjacent-averaging data smoothing for clarity.

2.4.2. Electron Microscopy

Scanning electron microscopy (SEM) experiments were performed on a JEOL 7400F microscope. High-angle annular dark-field scanning transmission electron microscopy (HAADF–STEM) and energy-dispersive X-ray spectroscopy (EDX) in STEM mode (STEM–EDX) studies were performed using an FEI Titan 80–200 Chemi-STEM microscope (200 kV, 0.08 nm point resolution, Super-X EDX detector). SEM measurements were also performed after treatment of the samples by either immersion in 1.0 M KOH for 1 h, or immersion for 2 h followed by electrolysis at potentials up to 1.45 V vs RHE for 10 mins each in 1.0 M KOH followed by rinsing with deionised water and drying in air.

2.4.3. X-ray Photoelectron Spectroscopy (XPS)

XPS measurements were performed using a monochromated microfocused Al K_α X-ray source that defined an analysis spot of ca. 650 × 400 μm. All spectra were acquired in normal emission with an enabled magnetic lens producing an effective analyser collection angle of ≈30°. Elemental regions were acquired at the nominal instrument resolution of 0.36 eV, with 0.1 eV step size. Charge neutralisation was provided by beams of low-energy (≤10 eV) Ar^+ ions and electrons guided by the magnetic lens; the aliphatic C 1s peak was observed at binding energy (BE) of 284.9±0.1 eV (FWHM of 1.3–1.8 eV) for all the samples, except for one case where a ca. 1 eV correction had to be applied. A convolution of Lorentzian and Gaussian lineshapes on a linear combination of Shirley and linear backgrounds was used to fit the individual components.

2.4.4. *In situ* and *Operando* Raman Spectroscopy

Measurements were performed using a Horiba LabRAM HR Evolution Raman spectrometer. A 532 nm frequency-doubled Nd:YAG (max power 23.6 mW) was used with a 50 × super-long working distance (SLWD) objective lens and a 600 grooves mm^{-1} spectral grating unless otherwise stated. Spectra obtained are the average of 30 spectral acquisitions of 10 s each at 25% total laser power constantly scanning over a circle of diameter 10 µm to minimise sample laser damage (DuoScan feature). Experiments were performed in 1.0 M KOH aqueous solution. Electrochemical measurements were performed using a potentiostat (PG128N, Autolab) and a purpose-built PEEK electrochemical cell. A $Ag|AgCl|KCl_{(sat)}$ reference electrode and a Pt wire counter electrode were used. The samples were allowed to equilibrate for two hours *in situ* prior to the application of a potential, as this was observed to be sufficient for the Raman spectra to reach a steady state at open circuit potential and thus surface reactions to complete. After this equilibration, potentials of interest were held for 10 minutes, with the Raman spectroscopy measurement performed during the second half of this.

3. Results and Discussion

3.1. Synthesis and Characterisation of CoP and AlCoP

The aluminium-modified cobalt phosphide (**AlCoP**) was synthesised by an analogous procedure to that previously reported for AlNiP,[3] with successive layers of Al and Co sputtered onto a free-standing Co foam, followed by heat treatment at 600 °C under Ar to ensure elemental mixing (resulting XRD pattern in Figure S1b), and then a phosphorisation process at 500 °C under Ar. Control **CoP** electrodes were synthesised by an identical procedure, with the omission of the Al sputtering step.

The prepared electrodes were first characterised by XRD (see Figure S1). According to the XRD analysis (Figure S1d), the as-synthesised **AlCoP** sample was a phase mixture of approximately 80% of Co_2P (ICDD no. 01-070-8359, orthorhombic, *Pnma*) and 20% of CoP (ICDD no. 03-065-2593, orthorhombic, *Pnma*), with a small amount of $Al(OH)_3 \cdot 3H_2O$ (most likely from AlP decomposition). XRD analysis of **CoP** also reveals a similar mixture of Co_2P and CoP phases (Figure S1c, Supporting Information).

Electron microscopy and EDX analysis were also performed on the as-prepared samples. Figure 1a shows the morphology of the **AlCoP** anode imaged by SEM, indicating the presence of micrometre-sized particles on the foam structure. A similar morphology is observed for the control **CoP** electrode foam (Figure S2). The distribution of Al is relatively uniform across the **AlCoP** particles, with no evidence of phase separation (Figure 1f). Table S1 summarises the composition of Co, P and Al in the **CoP** and **AlCoP** samples measured by EDX analysis. The elemental ratios of Co/P of between approximately 2:1 and 1:1 suggest that the electrodes mainly comprise Co_2P and CoP phases, consistent

with the XRD analysis. Interestingly, the presence of Al appears to have a significant impact on the elemental composition, leading to a higher Co/P ratio for **AlCoP**. Additional EDX analysis yields a Co/Al ratio of approximately 6:1 compared to 30:1 in the unmodified **CoP** control (Table S1). Representative EDX spectra of Al:CoP and Al:Co_2P regions of the **AlCoP** sample are presented in Figure S3, in which the phase-dependent features can be identified from the intensity variation of the Co-*L* and Co-*K* peaks.

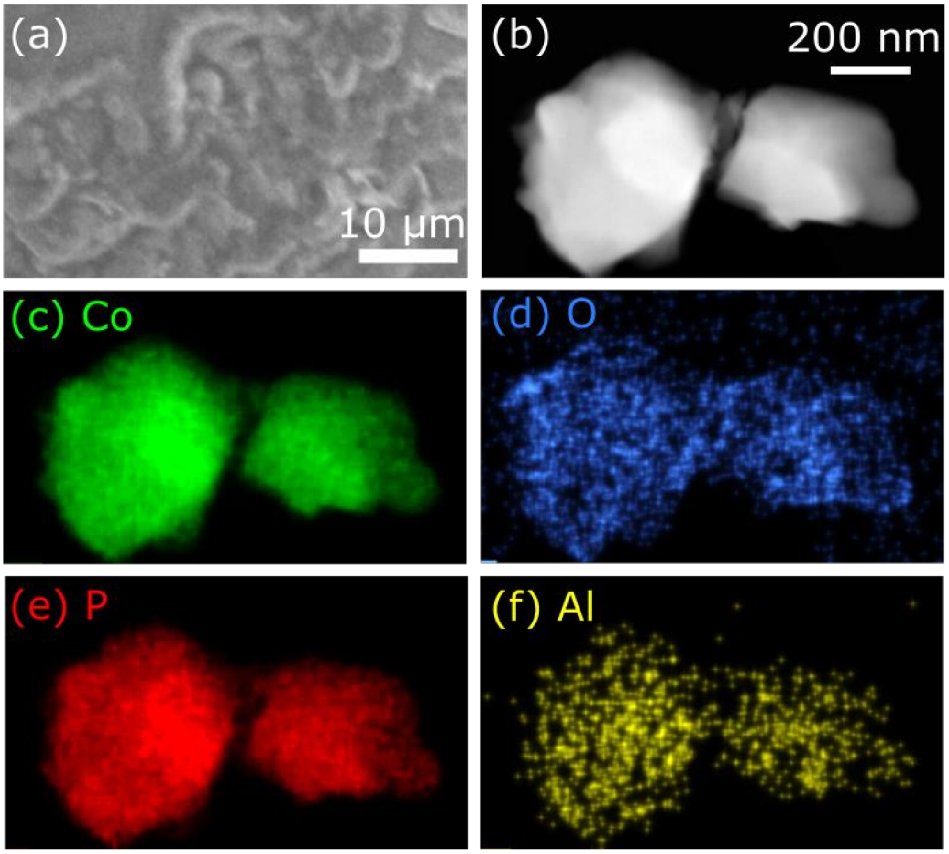

Figure 1 (a) SEM image of **AlCoP**. (b) HAADF–STEM image of two **AlCoP** particles along with EDX maps of (c) Co, (d) O, (e) P and (f) Al.

3.2. Electrochemical Performance of CoP and AlCoP as OER Anodes

Figure 2 summarises the electrochemical water oxidation performance in 1.0 M KOH of the prepared **AlCoP** and **CoP** anodes and compares them with pure Co. The **AlCoP** anode offers the most favourable OER characteristics, with current densities (j) of 10, 100, and 200 mA cm^{-2} reached at overpotentials (η) of approximately 270, 330, and 360 mV, respectively, in the cyclic voltammograms shown in Figure 2a. By comparison, the unmodified **CoP** anode exhibits more positive OER overpotentials by up to 50 mV at the highest current density measured. The Al-free and Al-modified anodes have comparable Tafel slopes (T_S) of 45 mV dec^{-1} and 38 mV dec^{-1}, respectively (Figure 2b), suggesting that the Al

introduction does not drastically alter the OER mechanism or intrinsic activity per active site. The activity of the Co-based catalysts was also compared to standard PGM reference catalysts, IrO_2 and RuO_2 (Figure S4).[17] The onset of OER for the reference catalysts is between that of **AlCoP** and **CoP**, and therefore, despite possible differences in surface area between **AlCoP** and the IrO_2 and RuO_2 catalysts, it can be said that the former offers at least a comparable OER overpotential to the significantly more expensive and less abundant reference catalysts.

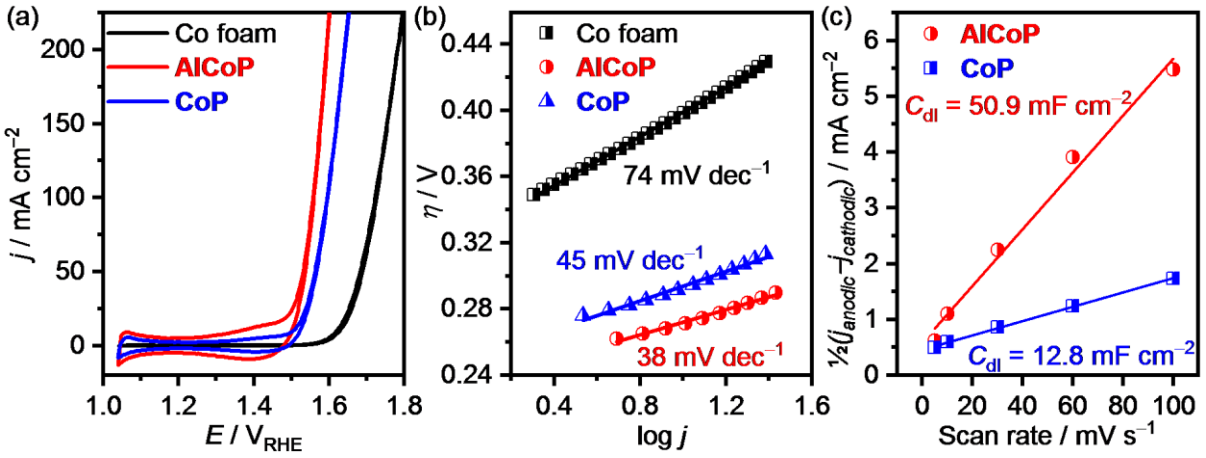

Figure 2 (a) Cyclic voltammetry (5 mV s^{-1}) (b) Tafel plots and (c) geometric double-layer capacitance plots for synthesised foam anodes. All recorded in 1.0 M KOH at room temperature.

The larger capacitive currents observed for **AlCoP** between approximately 1.3 and 1.5 V in Figure 2a are indicative of a substantially larger ECSA which likely explains its apparent enhanced OER performance based on geometric area. Double-layer capacitance, C_{dl}, measurements in this potential region (Figure 2c) confirm that the ECSA of **AlCoP** is higher than that of **CoP** by approximately a factor of four. In order to deconvolute the effect of ECSA and establish how the intrinsic OER activities of **CoP** and **AlCoP** compare, the CV data in Figure 2a was normalised to the measured double-layer capacitance (Figure S5). From this it is evident that the observed increase in absolute activity of **AlCoP** per geometric area compared to **CoP** is due to an *in situ* increase in ECSA upon exposure to alkaline electrolyte solution, despite the intrinsic activity of **CoP** (per unit ECSA) being marginally higher. However, this normalisation approach retains the limitations of (a) assuming that both materials have a similar specific capacitance, which may not be true under the alkaline conditions of the electrochemical testing and (b) neglecting the contribution of cation intercalation into the material.[18]

In addition to the low overpotential OER displayed in the CV and shallow Tafel slope, the **AlCoP** anode also demonstrates stable long-term performance, with the chronopotentiometry at 10 mA cm^{-2} in 1.0 M

KOH solution (current density chosen for comparison with literature[19]) shown in Figure S6. It was found that the OER overpotential of below 1.48 V was retained for at least 150 h with no sign of deterioration, demonstrating the potential of this material in electrolysis applications.

3.3. Surface Changes During OER

In order to better understand the origin of the different relative ECSA measured for **CoP** and **AlCoP** it is important to consider physical and chemical changes occurring at the surface of the catalyst resulting from immersion in strongly alkaline solution and polarisation to anodic potentials. *Ex situ* SEM imaging and XPS and XRD analyses were therefore performed to establish the nature and extent of any such morphological and chemical changes, respectively.

3.3.1. SEM Imaging

The surface of the samples underwent significant surface morphological changes upon immersion in the 1.0 M KOH electrolyte solution. SEM images of as-prepared **CoP** and **AlCoP** are shown in Figure 3, revealing a fused particulate structure. The micrographs of both the **CoP** and **AlCoP** electrodes after immersion in the test solution exhibit major differences compared to the as-prepared samples, with well-defined platelets of approximately 500 nm diameter covering the surface. SEM imaging of samples exposed to OER testing conditions (Figure S7) reveal no further significant change in morphology, suggesting that the most substantial surface transformation occurs spontaneously upon exposure to the alkaline electrolyte solution. The appearance of the platelet morphology is similar to that of cobalt oxides previously studied for the OER[18], consistent with the rapid chemical oxidation of the **CoP** and **AlCoP** surface. There are subtle differences in the morphological changes induced by alkaline conditions between the **AlCoP** and control **CoP** samples, with the former exhibiting more rounded platelets while the latter show evidence of edge-faceting. This may point towards different oxidation or dissolution behaviours, but a true statistical comparison of the surfaces was not possible and it is plausible that the significantly increased ECSA of **AlCoP** is due to differences at the sub-10 nm scale, and are beyond the spatial resolution of the SEM measurement. In addition, the relative ECSA is measured *in situ*, compared to *ex situ* SEM, and the differences between the samples is likely only to be present when the electrodes are immersed in the OER electrolyte solution.

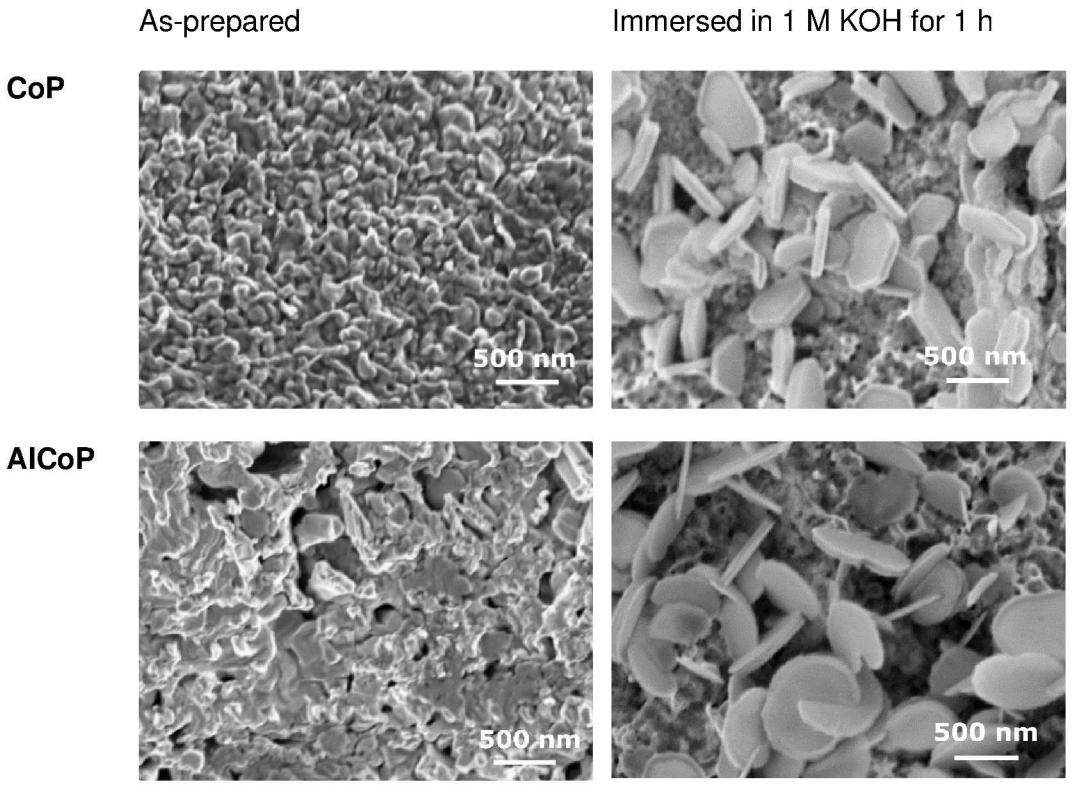

Figure 3 SEM of **CoP** and **AlCoP** as-prepared and after immersion in 1 M KOH solution for 1 h. Micrographs are chosen as representative of the entire sample.

3.3.2. XPS Analysis

XPS was next used to examine the surface chemical composition of the **CoP** and **AlCoP** anodes (Figure 4). In agreement with analogous phosphorisation of Ni-based materials,[1,2,20] as-prepared **AlCoP** and **CoP** exhibit P/Co ratios in the 2.5–3 range, suggesting that the phosphorisation step efficiently deposits a few-nm-thick surface layer of excess P, which becomes oxidised into phosphates, as evidenced by the P $2p_{3/2}$ component at 133.9±0.1 eV,[1,2,20,21] the total O/P ratios of approximately 3–4, and the O 1s spectral envelope (two components at 531.6±0.2 eV and 533.2±0.2 eV).[1,20] After stability testing for 150 h, this phosphate layer almost completely disappears from the **AlCoP** surface (Figure 4d), as with NiP,[20] AlNiP,[1] and MgNiP,[2] suggesting dissolution of the phosphate material in aqueous solution.

The presence of Al in the **AlCoP** samples is unaffected by exposure to OER conditions, with an Al/Co elemental ratio of approximately 2 observed by XPS in **AlCoP** both before and after electrolysis for 150 h in 1.0 M KOH. This is in addition to EDX analysis (Figure S8 and Table S1) of the bulk **AlCoP** before and after this stability testing, which reveals no significant change in the Co/Al ratio (between 5:1 and 6:1). Therefore, it can be concluded that Al is not lost from the material during immersion and polarisation in alkaline aqueous solution from either the surface or the bulk (from XPS and EDX measurements, respectively), which is in stark contrast with previously-studied AlNiP, where Al was depleted from the bulk after electrochemical testing and was not observable on the surface.[1] Since no

significant Al leaching is observed for **AlCoP**, this mechanism cannot be used to rationalise the increased ECSA observed for this material.

The transformation of the surface chemistry to predominantly metal hydroxide after electrochemical testing has previously been indicated for NiP[20] and AlNiP[1] based on a combination of the Ni 2p and O 1s spectral signatures. For **AlCoP**, the changes in SEM images discussed above indicate a complete change in surface properties, whereas similar evidence from XPS is only obtained from the loss in P 2p signal, in part because the Co $2p_{3/2}$ binding energies (BE) and lineshapes are less sensitive to the precise chemical state or environment than they are for core levels of other transition metals, such as Ni,[1,2,20,22,23] Cu,[22,24] or Mo.[22,25]

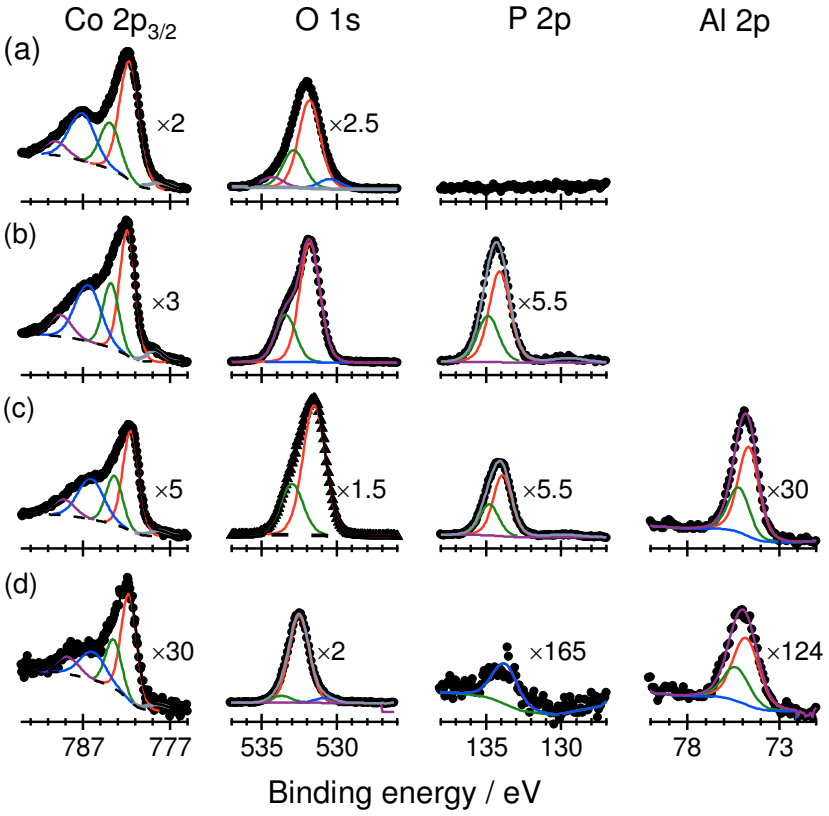

Figure 4 XPS characterisation of **CoP** and **AlCoP**. The spectral signatures correspond to: (a) the initial Co foam, (b) **CoP**, (c) **AlCoP**, and (d) **AlCoP** after OER for 150 h. Spectra in Co $2p_{3/2}$, O 1s, P 2p and Al 2p regions are shown for each element as raw intensities, multiplied by the indicated factors to simplify visual comparison; symbols = raw data, dashed lines = background, coloured lines = fit components, thick black lines = overall fit.

The main unambiguous conclusion about the Co chemistry in all the materials in Figure 4 is the absence of any significant quantity of Co^{3+}, which would be associated with qualitatively different lineshapes of the Co $2p_{3/2}$ satellites and lower BE for O 1s.[13,22] The main Co $2p_{3/2}$ component (red line in Co $2p_{3/2}$ fits, Figure 4) at BE of 781.7±0.2 eV with satellites at ca. 786.5 and 789.7 eV is more characteristic of Co^{2+},[22] including in nanostructured Co phosphides oxidized into phosphates and hydroxides.[26–28] The small feature at ca. 778 eV BE (grey line in Co $2p_{3/2}$ fits, Figure 4) is not diagnostic of any specific compound, as it could correspond to any combination of contributions from Co phosphide,[26–28] Co metal, or even an overlapping Auger peak.[22] Likewise, the Co $2p_{3/2}$ component at 783.7±0.2 eV (green lines in Co $2p_{3/2}$ fits, Figure 4) does not imply a distinct chemical compound: resolving the Co $2p_{3/2}$ spectra at that level requires advanced synchrotron-based measurements.[29] Finally, we note that the main O 1s component at ca. 532.5 eV after CV testing of **AlCoP** is associated with an increase in C–O chemistry[30] of the organic overlayer from sample handling, rather than with changes in Co chemistry.

3.4. X-ray Diffraction

XRD was used to identify any bulk chemical changes caused by immersion and anodic polarisation of the **AlCoP** electrodes in KOH. XRD patterns of the as-prepared **AlCoP** electrodes and the same electrode after extensive OER testing for 150 h in 1.0 M KOH are shown in Figures S1d and S1e. Two distinct differences are observed: (i) the Co_2P phase is retained in the bulk **AlCoP** after extensive electrocatalysis and (ii) the CoP phase present in the as-prepared **AlCoP** sample has a significantly reduced intensity after OER testing. These results indicate that despite the surface changes shown by XPS and SEM, the bulk of the **AlCoP** foam electrodes remain as cobalt phosphide. Since XRD is not a surface-sensitive technique, it was not possible to chemically characterise the surface species using this method. Instead surface-sensitive Raman spectroscopy was utilised to unravel the reason behind the observed increased ECSA of the **AlCoP** electrodes.

3.5. Raman Spectroscopy of CoP and AlCoP Anodes under *Ex Situ*, *In Situ* and *Operando* Conditions

Raman spectroscopy was used to further elucidate the differing surface chemical speciation of the **CoP** and **AlCoP** materials and to probe in more detail the origin of the differences in OER performance caused by the Al modification. Initial *ex situ* Raman spectra recorded in air exhibit a collection of intense bands in the range 100 cm^{-1} to 480 cm^{-1} for both **CoP** and **AlCoP**, which are consistent with previous reports and can be assigned to T_g, E_g and A_g vibrational modes within the cobalt phosphide structure (Figure 5a).[31–33] Inspection of the band positions (Table S2), indicates that the majority of the **CoP** bands are slightly shifted to lower wavenumber by the addition of Al.

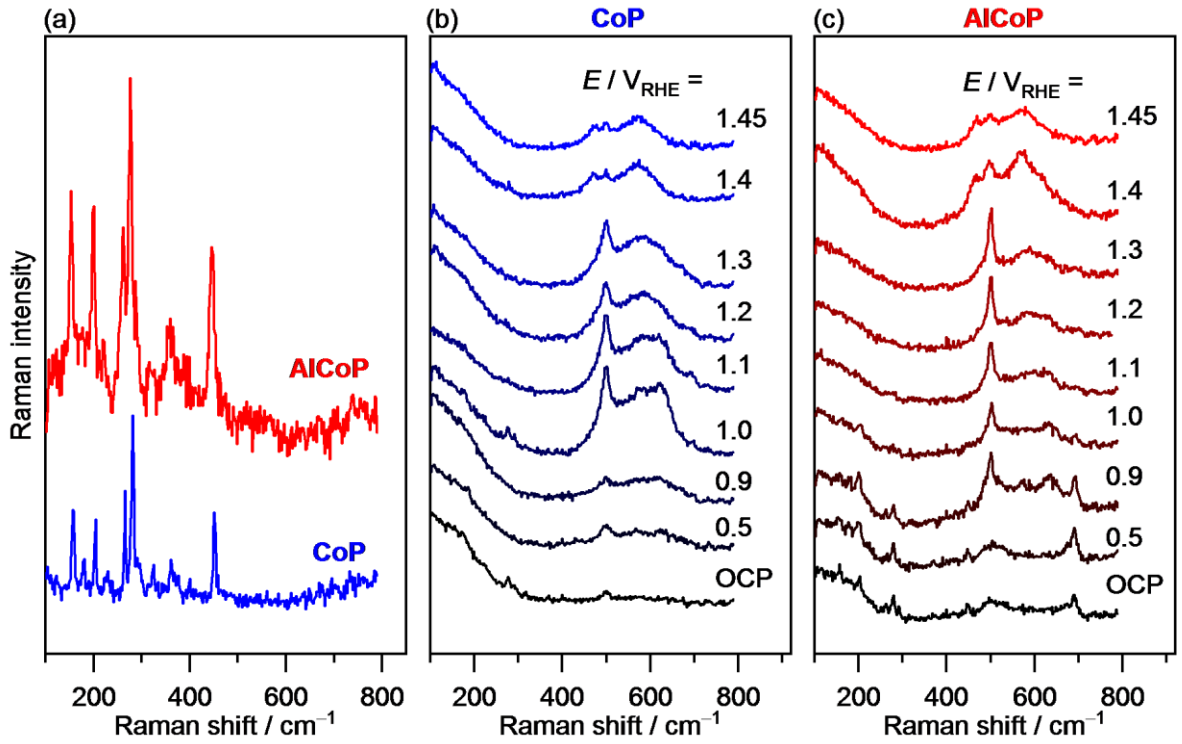

Figure 5 (a) Raman spectra of **CoP** and **AlCoP**, recorded in air. Raman spectra of (b) **CoP** and (c) **AlCoP** recorded at various potentials, including the OCP (~0.2 V_{RHE}), in 1.0 M KOH.

Changes in the surface chemical structure of **CoP** and **AlCoP** in the alkaline environment used in the electrochemical tests were evaluated by Raman measurements performed with the electrodes submerged in 1.0 M KOH solution. Figure 5b and Figure 5c (lowermost spectra) show Raman spectra recorded at OCP (approximately 0.2 V_{RHE}). Almost complete attenuation of the phosphide peaks in the 100 cm^{-1} to 480 cm^{-1} range occurs for both materials, and in both cases growth of a new feature at 500 cm^{-1} is observed. Furthermore, in the case of **AlCoP** only, a distinct band centred at 690 cm^{-1} is also formed. The 500 cm^{-1} peak was ubiquitous to all areas of both samples under these conditions, and is characteristic of CoO(OH).[34–36] The sharp band observed at 690 cm^{-1} only for **AlCoP** is highly diagnostic of spinel structures, with Co_3O_4[35,37,38] and Al/Co mixed oxide[39,40] spinel structures reported to exhibit Raman peaks in this region, although the precise Al/Co ratio cannot be determined by Raman spectroscopy in this context. Both Co_3O_4 and Al_2CoO_4 spinel materials are isostructural, with near-identical lattice constants,[41] and hence, given that this 690 cm^{-1} peak is only observed in the presence of Al, it is probable that Al induces a preference for a crystalline spinel phase based on its propensity to form the mixed oxide spinel structures with Co.[39]

It is widely understood that the surface metal oxide/oxyhydroxide is the dominant OER active phase in phosphide electrocatalysts,[1,7,35,42] so it is reasonable to assert that the differing oxidation behaviour of

the phosphide materials noted above likely plays an important role in their differing electrochemical performance. Therefore, to gain a better understanding of the surface chemistry under active conditions, Raman spectroscopy was performed with the sample under oxidising potentials. Figure 5b-c show Raman spectra as the substrate potential is successively taken more positive from OCP to 1.45 V_{RHE}, the onset of OER. It was not possible to record Raman spectra at more positive potentials than this due to rapid bubble formation. The behaviour of two materials is broadly similar but shows some clear differences at potentials approaching the OER. Upon application of moderately positive potentials, the spinel peak (690 cm^{-1}) for **AlCoP** diminishes before disappearing at 1.1 V_{RHE}. Above 1.0 V_{RHE}, the peak at 500 cm^{-1} for both compounds sharpens and increases in intensity alongside a broad band at around 630 cm^{-1}, also associated with CoO(OH),[18] before diminishing somewhat above 1.3 V_{RHE}. At potentials above 0.9 V_{RHE}, a broad peak at 580 cm^{-1} grows for both compounds, assigned to amorphous CoO_x,[37,43] although this peak is markedly more prominent relative to the CoO(OH) peak in the case of **CoP**.

At potentials of 1.4 V_{RHE} and above (at the onset of OER), the spectra from **CoP** and **AlCoP** become effectively indistinguishable. The CoO(OH) peak at 500 cm^{-1} is still present, alongside a new peak at 475 cm^{-1} and the broad peak at 580 cm^{-1}. The latter two have previously been assigned to CoO_2[35] and are also present in partially-delithiated $LiCoO_2$.[44] Since the formation of bubbles from the electrode surface (presumably from the OER) was also observed from E = 1.4 V_{RHE}, it is therefore apparent that during oxygen evolution both CoO(OH) and CoO_2-related phases are present for **CoP** and **AlCoP**, in accordance with previous reports.[35,45] CoO_2 has been proposed as the active OER species in previous studies on cobalt oxides, and delithiated $LiCoO_2$ has been shown as an active OER catalyst under these highly alkaline conditions,[46] so it is likely that a CoO_2-related phase is responsible for the observed OER catalysis. The key differences in the *in situ* and *operando* spectra of **CoP** and **AlCoP** is therefore the presence of a spinel phase in the case of **AlCoP** upon immersion in KOH solution, compared to a more pronounced amorphous CoO_x signal for **CoP**.

It is clear from the *operando* Raman spectroscopy measurements that, whilst both **CoP** and **AlCoP** materials likely share a common catalytically-active CoO_2 phase under OER conditions, the route by which this phase is formed differs considerably – **CoP** forms an intermediate amorphous CoO_x phase, whilst **AlCoP** is oxidised *via* a distinct crystalline spinel phase. A previous study found that spinel Co_3O_4 films exhibit a higher ECSA by a factor of six than compared to CoOOH films prepared from identical $Co(OH)_2$ precursors.[18] This is explained by the smaller unit cell (per Co atom) of the spinel Co_3O_4 compared to other Co oxides, and thus shrinkage upon Co_3O_4 formation causes cracks and pores, and therefore a higher surface area. In the case of **AlCoP**, we observe the formation of a Co/Al oxide spinel, which is similarly compact since the lattice parameters of both Co_3O_4 and Al_2CoO_4 are nearly identical (8.0835 Å and 8.0968 Å, respectively[41]). We therefore propose that the Al-induced spinel formation observed in this catalyst causes the same shrinkage upon electrolyte exposure, thus resulting

in the higher surface area of the catalyst derived from **AlCoP** and the apparent increase in OER performance per unit geometric area. Whilst this mechanism is similar to the previously-described Co oxide catalyst,[18] the absolute performance of our phosphide-derived catalyst is much higher, due to the foam structure offering a high macroscopic surface area and also the established reduction in overpotential owing to the underlying Co phosphide, the presence of which is confirmed by post-catalysis XRD.[47] It is worth highlighting here that the bulk phosphide phase ratio does change after exposure to OER conditions, with loss of the CoP phase from the XRD pattern being considerably more pronounced than Co_2P, however it is unclear whether the CoP phase simply dissolves from the surface or whether this phase is the specific precursor to the active oxide catalyst. Finally, we note that the mechanism of catalytic performance enhancement by Al reported here is in contrast to that recently proposed by Hung *et al.* for Fe-doped cobalt phosphide, who presented evidence of stabilisation of the phosphide phase by Fe.[48] This difference highlights the sensitivity of the chemical behaviour of the catalyst under alkaline conditions to the specific dopant-host interaction.

4. Conclusions

Surface modification of a porous cobalt phosphide foam with Al results in a high current density, low overpotential OER catalyst, reaching a current density of 200 mA cm^{-2} at an overpotential of 360 mV, 50 mV lower than the Al-free control. This increased performance can be ascribed to the increased ECSA of the Al-modified material. Al-derived ECSA enhancement has been previously observed for nickel phosphide materials, but this Co phosphide study has identified a different mechanism to the Al dissolution described previously. In the case of **AlCoP**, the Al content is retained upon exposure to alkaline electrolyte solution, and instead the *in situ* oxidation of the surface to the active CoO_2 catalyst occurs *via* a spinel intermediate, the more compact crystal structure of which causes shrinking of the material and therefore cracks on the nanoscale. This spinel intermediate was not observed for **CoP**, which oxidises *via* an amorphous phase, suggesting that Al incorporation plays a key role in favouring the crystalline spinel structure and the resulting increased surface area.

Furthermore, this work highlights the effectiveness of *in situ* and *operando* Raman spectroscopy, combined with *ex situ* surface analysis for identifying subtle differences in surface chemistry which have a strong effect on electrocatalyst performance. By providing new insights into the underlying basis of the performance enhancement, this work is expected to support the potential implementation of the Al-modification strategy to other catalytic materials systems.

Conflicts of Interest

There are no conflicts of interest to declare.

Acknowledgements

The authors would like to thank Dr. J. Xu for his help with electrochemical measurements. This project has received funding from the European Union's Horizon 2020 research and innovation programme under grant agreement No. 686053. TER and AJW also acknowledge the National Measurement System of the UK Department of Business, Energy and Industrial Strategy.

References

1 J. Xu, J. P. S. Sousa, N. E. Mordvinova, J. D. Costa, D. Y. Petrovykh, K. Kovnir, O. I. Lebedev and Yu. V. Kolen'ko, *ACS Catal.*, 2018, **8**, 2595–2600.

2 J. Xu, X.-K. Wei, J. D. Costa, J. L. Lado, B. Owens-Baird, L. P. L. Gonçalves, S. P. S. Fernandes, M. Heggen, D. Y. Petrovykh, R. E. Dunin-Borkowski, K. Kovnir and Yu. V. Kolen'ko, *ACS Catal.*, 2017, **7**, 5450–5455.

3 J. L. Lado, X. Wang, E. Paz, E. Carbó-Argibay, N. Guldris, C. Rodríguez-Abreu, L. Liu, K. Kovnir and Yu. V. Kolen'ko, *ACS Catal.*, 2015, **5**, 6503–6508.

4 Y. Shi and B. Zhang, *Chem. Soc. Rev.*, 2016, **45**, 1529–1541.

5 H. Du, R.-M. Kong, X. Guo, F. Qu and J. Li, *Nanoscale*, 2018, **10**, 21617–21624.

6 J. F. Callejas, C. G. Read, C. W. Roske, N. S. Lewis and R. E. Schaak, *Chem. Mater.*, 2016, **28**, 6017–6044.

7 J. Chang, Y. Xiao, M. Xiao, J. Ge, C. Liu and W. Xing, *ACS Catal.*, 2015, **5**, 6874–6878.

8 K. Liu, C. Zhang, Y. Sun, G. Zhang, X. Shen, F. Zou, H. Zhang, Z. Wu, E. C. Wegener, C. J. Taubert, J. T. Miller, Z. Peng and Y. Zhu, *ACS Nano*, 2018, **12**, 158–167.

9 E. J. Popczun, J. R. McKone, C. G. Read, A. J. Biacchi, A. M. Wiltrout, N. S. Lewis and R. E. Schaak, *J. Am. Chem. Soc.*, 2013, **135**, 9267–9270.

10 Z. Huang, Z. Chen, Z. Chen, C. Lv, M. G. Humphrey and C. Zhang, *Nano Energy*, 2014, **9**, 373–382.

11 E. J. Popczun, C. W. Roske, C. G. Read, J. C. Crompton, J. M. McEnaney, J. F. Callejas, N. S. Lewis and R. E. Schaak, *J. Mater. Chem. A*, 2015, **3**, 5420–5425.

12 D.-H. Ha, B. Han, M. Risch, L. Giordano, K. P. C. Yao, P. Karayaylali and Y. Shao-Horn, *Nano Energy*, 2016, **29**, 37–45.

13 P. T. Babar, A. C. Lokhande, B. S. Pawar, M. G. Gang, E. Jo, C. Go, M. P. Suryawanshi, S. M. Pawar and J. H. Kim, *Appl. Surf. Sci.*, 2018, **427**, 253–259.

14 S. H. Yu and D. H. C. Chua, *ACS Appl. Mater. Interfaces*, 2018, **10**, 14777–14785.

15 R. Zhang, C. Tang, R. Kong, G. Du, A. M. Asiri, L. Chen and X. Sun, *Nanoscale*, 2017, **9**, 4793–4800.

16 X. Lv, Z. Hu, J. Ren, Y. Liu, Z. Wang and Z. -Y. Yuan, *Inorg. Chem. Front.*, 2019, **6**, 74–81.

17 D. K. Mann, J. Xu, N. E. Mordvinova, V. Yannello, Y. Ziouani, N. González-Ballesteros, J. P. S. Sousa, O. I. Lebedev, Yu. V. Kolen'ko and M. Shatruk, *Chem. Sci.*, 2019, **10**, 2796–2804.

18 Y.-C. Liu, J. A. Koza and J. A. Switzer, *Electrochim. Acta*, 2014, **140**, 359–365.

19 C. C. L. McCrory, S. Jung, J. C. Peters and T. F. Jaramillo, *J. Am. Chem. Soc.*, 2013, **135**, 16977–

16987.

20 X. Wang, W. Li, D. Xiong, D. Y. Petrovykh and L. Liu, *Adv. Funct. Mater.*, 2016, **26**, 4067–4077.

21 R. Franke, T. Chassé, P. Streubel and A. Meisel, *J. Electron Spectros. Relat. Phenomena*, 1991, **56**, 381–388.

22 M. C. Biesinger, B. P. Payne, A. P. Grosvenor, L. W. M. Lau, A. R. Gerson and R. S. C. Smart, *Appl. Surf. Sci.*, 2011, **257**, 2717–2730.

23 M. Salimian, M. Ivanov, F. L. Deepak, D. Y. Petrovykh, I. Bdikin, M. Ferro, A. Kholkin, E. Titus and G. Goncalves, *J. Mater. Chem. C*, 2015, **3**, 11516–11523.

24 E. Carbó-Argibay, X.-Q. Bao, C. Rodríguez-Abreu, M. Fátima Cerqueira, D. Y. Petrovykh, L. Liu and Y. V. Kolen'ko, *J. Colloid Interface Sci.*, 2015, **456**, 219–227.

25 X.-Q. Bao, D. Y. Petrovykh, P. Alpuim, D. G. Stroppa, N. Guldris, H. Fonseca, M. Costa, J. Gaspar, C. Jin and L. Liu, *Nano Energy*, 2015, **16**, 130–142.

26 X. Chen, X. Ding, C. Wang, Z. Feng, L. Xu, X. Gao, Y. Zhai and D. Wang, *Nanoscale*, 2018, **10**, 13694–13701.

27 R. Luo, C. Liu, J. Li, J. Wang, X. Hu, X. Sun, J. Shen, W. Han and L. Wang, *J. Hazard. Mater.*, 2017, **329**, 92–101.

28 K.-L. Yan, X. Shang, L.-M. Zhang, B. Dong, Z.-Z. Liu, J.-Q. Chi, W.-K. Gao, Y.-M. Chai and C.-G. Liu, *Electrochim. Acta*, 2017, **249**, 16–25.

29 Y. Han, S. Axnanda, E. J. Crumlin, R. Chang, B. Mao, Z. Hussain, P. N. Ross, Y. Li and Z. Liu, *J. Phys. Chem. B*, 2018, **122**, 666–671.

30 E. H. Lock, D. Y. Petrovykh, P. Mack, T. Carney, R. G. White, S. G. Walton and R. F. Fernsler, *Langmuir*, 2010, **26**, 8857–8868.

31 A. Goryachev, L. Gao, Y. Zhang, R. Y. Rohling, R. H. J. Vervuurt, A. A. Bol, J. P. Hofmann and E. J. M. Hensen, *ChemElectroChem*, 2018, **5**, 1230–1239.

32 F. H. Saadi, A. I. Carim, W. S. Drisdell, S. Gul, J. H. Baricuatro, J. Yano, M. P. Soriaga and N. S. Lewis, *J. Am. Chem. Soc.*, 2017, **139**, 12927–12930.

33 L. Su, X. Cui, T. He, L. Zeng, H. Tian, Y. Song, K. Qi and B. Y. Xia, *Chem. Sci.*, 2019, **10**, 2019–2024.

34 J. Yang, H. Liu, W. N. Martens and R. L. Frost, *J. Phys. Chem. C*, 2010, **114**, 111–119.

35 N. Kornienko, N. Heidary, G. Cibin and E. Reisner, *Chem. Sci.*, 2018, **9**, 5322–5333.

36 B. S. Yeo and A. T. Bell, *J. Am. Chem. Soc.*, 2011, **133**, 5587–5593.

37 J. Tyczkowski, R. Kapica and J. Łojewska, *Thin Solid Films*, 2007, **515**, 6590–6595.

38 V. G. Hadjiev, M. N. Iliev and I. V Vergilov, *J. Phys. C Solid State Phys.*, 1988, **21**, L199–L201.

39 T. Fan, L. Dou and H. Zhang, *RSC Adv.*, 2016, **6**, 110274–110287.

40 A. Dandapat and G. De, *ACS Appl. Mater. Interfaces*, 2012, **4**, 228–234.

41 M. G. Brik, A. Suchocki and A. Kamińska, *Inorg. Chem.*, 2014, **53**, 5088–5099.

42 A. Dutta and N. Pradhan, *J. Phys. Chem. Lett.*, 2017, **8**, 144–152.

43 D. Gallant, M. Pézolet and S. Simard, *J. Phys. Chem. B*, 2006, **110**, 6871–6880.

44 C. M. Julien and A. Mauger, *AIMS Mater. Sci.*, 2018, 5, 650–698.

45 M. Mathankumar, S. Anantharaj, A. K. Nandakumar, S. Kundu and B. Subramanian, *J. Mater. Chem. A*, 2017, **5**, 23053–23066.

46 Z. Lu, H. Wang, D. Kong, K. Yan, P.-C. Hsu, G. Zheng, H. Yao, Z. Liang, X. Sun and Y. Cui, *Nat. Commun.*, 2014, **5**, 4345.

47 L. Ai, Z. Niu and J. Jiang, *Electrochim. Acta*, 2017, **242**, 355–363.

48 S. -F. Hung, Y. Zhu, G. -Q. Tzeng, H. -C. Chen, C. S. Hsu, Y. -F. Liao, H. Ishii, N. Hiraoka and H. M. Chen, *ACS Energy Lett.*, 2019, **4**, 2813–2820.